Low-energy electron diffraction from ferroelectric surfaces: Dead layers and surface dipoles in clean Pb(Zr,Ti)O_3(001)

Cristian M. Teodorescu,* Lucian Pintilie, Nicoleta G. Apostol, Ruxandra M. Costescu, George A. Lungu, Luminiţa Hrib, and Lucian Trupină
National Institute of Materials Physics, Atomiştilor 405A, 077125 Măgurele-Ilfov, Romania

Liviu C. Tănase, Ioana C. Bucur, and Amelia E. Bocîrnea
National Institute of Materials Physics, Atomiştilor 405A, 077125 Măgurele-Ilfov, Romania
and University of Bucharest, Faculty of Physics, Atomiştilor 405, 077125 Măgurele-Ilfov, Romania
(Received 11 April 2017; revised manuscript received 27 June 2017; published 19 September 2017)

The positions of the low energy electron diffraction (LEED) spots from ferroelectric single crystal films depend on its polarization state, due to electric fields generated outside of the sample. One may derive the surface potential energy, yielding the depth where the mobile charge carriers compensating the depolarization field are located (δ). On ferroelectric Pb(Zr,Ti)O_3(001) samples, surface potential energies are between 6.7 and 10.6 eV, and δ values are unusually low, in the range of 1.8 ± 0.4 Å. When δ is introduced in the values of the band bending inside the ferroelectric, a considerably lower value of the dielectric constant and/or of the polarization near the surface than their bulk values is obtained, evidencing either that the intrinsic 'dielectric constant' of the material has this lower value or the existence of a 'dead layer' at the free surface of clean ferroelectric films. The inwards polarization of these films is explained in the framework of the present considerations by the formation of an electron sheet on the surface. Possible explanations are suggested for discrepancies between the values found for surface potential energies from LEED experiments and those derived from the transition between mirror electron microscopy and low energy electron microscopy.

DOI: 10.1103/PhysRevB.96.115438

I. INTRODUCTION

Ferroelectric thin films are nowadays synthesized with advanced methods, yielding flat, single crystalline and in most cases single domain structures, with well-defined out-of-plane polarization. Such systems allow one to determine fundamental aspects of the material together with the intimate processes occurring at its interfaces with metals. It was shown more than one decade ago that, in order to stabilize the single-domain state, the depolarization field inside the ferroelectric must be compensated by the accumulation of mobile charge carriers near the external surfaces [1,2]. Inside the ferroelectric, a surface band bending VB occurs due to the combined effect of the depolarization field and mobile charge accumulation, which may be expressed as:

$$V_B = -\frac{eP\delta}{\epsilon_0 \epsilon_r}, \tag{1}$$

where e is the elemental charge, P is the value of the out-of-plane polarization (positive when oriented outwards), δ is the distance from the surface to the center of the mobile charge sheet, ϵ_0 is the permittivity of vacuum, and ϵ_r the dielectric constant of the film. Films presenting polarization oriented outwards ($P^{(+)}$) present a bending of energy bands towards lower energies (or larger binding energies) near the surface, while films with $P^{(-)}$ polarization present a band bending towards higher energies (lower binding energies). Interface barriers may be derived by the Schottky-Simmons formalism using temperature-dependent I–V curves [3]; band bending at ferroelectric surfaces is investigated by using x-ray photoelectron spectroscopy (XPS), by assuming that core level positions are rigidly shifted with the vacuum level [4–7]. This was further confirmed by photoelectron spectromicroscopic imaging of ferroelectric surfaces with binding energy contrast [8]. Core level binding energy shifts of 0.6–1 eV are derived for a ferroelectric with strong out-of-plane polarization, Pb($Zr_{0.2}Ti_{0.8}$)O_3 (PZT) having $P \sim$ 0.8–1 Cm^{-2} [6,7]. Considering ϵ_r around 200, a value of δ of about 1.5–2 nm is obtained. But it is clear that for a ferroelectric with a nonlinear dependence $P(E)$ the definition of the dielectric constant is subject to some restrictions; metal contacts complicate further the problem due to interface dipoles and image charges. Studies of metals deposited on ferroelectrics revealed a wealth of phenomena, starting with negatively charged insulated metal particles [9] to nonuniform variations of the band bending as a function of the morphology [10,11].

Another hypothesis is that the charges needed to compensate the depolarization field are located *outside* the ferroelectric [12–14], external to the fixed charges, involving also adsorbed molecules. This produces a surface band bending oriented opposite to the above formula, with the δ parameter being this time the distance from the surface to the compensating charge sheet, irrespective of its origin. This model is used in graphene layers grown on ferroelectric surfaces [15,16], although in reality more complicated phenomena occur in the detected resistance hysteresis, involving contaminant molecules [17]. It will be of first aid for device engineering to clarify the origin of the surface band bending and the screening mechanism of the depolarization field.

Charge carriers that compensate the depolarization field in a thin ferroelectric film are generated by defects occurring during the synthesis of the film via a 'self-doping'

*teodorescu@infim.ro

mechanism [18]. One may imagine that the electric field outside the ferroelectric layer will be produced by the very thin region of the sample where the field of the elemental dipoles is not compensated by the field produced by the accumulated charge carriers. A way to evaluate this 'effective thickness' of the ferroelectric with respect to the field generated *outside* the sample may help to understand what is happening *inside* the ferroelectric. Furthermore, a correct quantification of the outer field may help in understanding the role played by ferroelectricity in the catalytic properties of these surfaces [19] and other charge transfer processes [20]. Since low energy electron diffraction (LEED) analyzes electrons scattered by the sample, this technique appears to be a good candidate for investigating the outer electric field produced by a ferroelectric.

An alternative way to tackle this problem, i.e., evaluate potential energies generated by the sample polarization towards the vacuum side of the surface of a ferroelectric is to use mirroring of low electrons. The transition from "mirror electron microscopy" to "low energy electron microscopy" (MEM–LEEM), i.e., from the case when electrons are deviated without touching the surface and the case of electrons interacting physically with the sample is reflected by a negative jump in the flux of reflected electrons recorded as a function of the electron kinetic energy [21–24]. The difference in energy between electrons reflected on areas with opposite out-of-plane polarization is then used to derive the potential of such a surface. The obtained values for this energy difference are unusually low, ranging from 60–90 meV for a 30 nm thick PZT grown on $SrTiO_3$(001) with a $SrRuO_3$ buffer layer [21], or about 100 meV for Mg-doped $LiNbO_3$(0001) single crystals [22], to 400 meV on $BaTiO_3$(001) single crystals [23], or 450 meV for 70 nm $BiFeO_3$ grown on (La,Sr)MnO_3 on $SrTiO_3$(001) [24]. These values are considerably lower than twice the band bending defined by Eq. (1) and confirmed by photoelectron spectroscopy. The difference in MEM–LEEM should be roughly on the order of on $ePd{\epsilon_0}^{-1}$, where d is some microscopic characteristic distance of variation of the surface potential (e.g., thickness of a layer with uncompensated dipoles). It is easy to evaluate that this should be ϵ_r times larger than the band bending inside the ferroelectric, if $d = \delta$. On the other hand, even if d is in the range of 1 Å, the order of magnitude of the surface potential energy exceeds 10 eV for $P \sim 1$ Cm^{-2}, thus the observed values are two orders of magnitude lower than the expected ones. There is no full explanation of this discrepancy: Some attempts invoke the effect of external screening charges [21,22], dead layers [24], or just simply the fact that the polarization of the outer shells of the ferroelectric is considerably lower, and the polarization of the inner shells is screened by the mobile charge sheets formed near the surface, according to the mechanism related to Eq. (1), discussed above.

Still unsettled problems in the field of ferroelectrics are related to the 'dielectric constant' of these materials (supposed as depending only on the material and not on its processing, morphology, geometry, or interfaces) and the 'dead layer' (low dielectric constant and/or polarization) at the free surface or at interfaces with metals. Most experimental and theoretical studies were focused on capacitor structures. The above mentioned dielectric constant in the range of several hundreds is used by most groups in the field of ferroelectrics; however, for PZT, theoretical calculations inferred lower values, such as 37 (c axis) or 67 (a axis) [25]. Raman spectroscopy proposed also static dielectric constants in the range of 41 (c axis) [26], while more recently a complex electrical investigation derived an 'intrinsic' dielectric constant of about 27–56, when all trapping and interface effects are properly taken into account [27]. Some reports claim that 'dead layers' are present, with negative impact on ferroelectric and dielectric properties, while other reports claim that there is no 'dead layer' and ferroelectric properties might be even enhanced at interfaces [28–35]. The thickness of the 'dead layer' was reduced from a few nm to 2–3 unit cells as the epitaxial quality of the investigated samples was improved [31,34,36]. Recent studies drew attention that the model of serial capacitors used to include the 'dead layer' effect might not be entirely appropriate [37]. Few studies tackle the problem of the 'dead layer' at the free surface of a ferroelectric sample [38–40]. If one considers a single domain epitaxial ferroelectric layer, it is clear that the properties of the surface layer will deviate from those of the bulk, especially if the layer is not contaminated and is placed in ultrahigh vacuum. The polarization, most probably, will gradually decay towards the surface [34], sometimes even promoting ultrathin layers with reversed polarization [28]. Also, at interfaces with metals, details of the chemical interaction between the first layers from the ferroelectric together with the charge screening mechanism in metals are shown to influence strongly the formation of 'dead layers' [28–30,33]. It results that the information regarding the finite thickness of this surface layer is of significant importance in understanding ultrathin ferroelectric layers and their heterostructures, in view of most applications [29,32].

Solutions for electron trajectories in the presence of a field generated by a ferroelectric material are not reported so far. Early electron diffraction evidence from ferroelectric samples can be traced to about two decades ago [41], mainly to pinpoint the heteroepitaxy mechanism. A pioneering work using detailed LEED I–V curves analyzes derived the formation of a permanent static dipole moment for the first surface layer (surface puckering) in a paraelectric $SrTiO_3$ [42]. A much more detailed LEED I–V curve analysis for (4 and 10 ML) $BaTiO_3$/(15 nm)$SrRuO_3$/$SrTiO_3$(001) (BTO/SRO/STO) synthesized by pulsed laser deposition (PLD) revealed sharp LEED patterns which were analyzed by multiple scattering analysis to yield upwards polarization [39]. We will show that similar information may be obtained from a much simpler analysis starting with the same LEED patterns recorded at different electron kinetic energies, without multiple scattering calculations [43]. Positively poled faces of a ferroelectric $LiNbO_3$(0001) were reported to exhibit similar LEED patterns as opposed faces, but images were not shown [44]. Other recent reports on LEED on ferroelectrics use this technique to assess the quality of the surfaces [45–48], the formation of a $(\sqrt{3} \times \sqrt{3})R30^\circ$ superstructure in $BaTiO_3$ synthesized by magnetron sputtering on Pt(111) [45] or other superstructures, such as $(\sqrt{5} \times \sqrt{5})R26.6^\circ$ and $(5\sqrt{2} \times \sqrt{2})R45^\circ$ due to different cation vacancy distributions in $Sr_{0.63}Ba_{0.37}Nb_2O_6$(001) single crystals [46].

In the following we shall quantify the effect on the trajectories of LEED electrons by a ferroelectric thin film and analyze the experimental results obtained on several films of different

thickness, by using two different LEED optics. The comparison between the surface band bending inside the film obtained by XPS and that outside the film, derived by LEED, will allow us to get more insight on the relevant parameters δ and ϵ_r.

II. THEORETICAL CONSIDERATIONS

A. Basic theory

The ferroelectric surface is modeled as a uniform surface density of elemental dipoles, extending over the z coordinate over the thickness d, as represented in Fig. 1. If $\mathbf{P}$ is the polarization, A the area of the surface, and d the thickness, the total dipole moment is $\mathbf{p}_{\text{tot}} = \mathbf{P}Ad$, and the dipole surface density is $\mathbf{P}\hat{A}\cdot d$. Let (x, y, z) be the coordinate of a point in space ($z > 0$) and $(x_0, y_0, 0)$ the coordinates describing the ferroelectric surface of area $(2l) \times (2l)$, such that $-l < x_0 < l$, $-l < y_0 < l$. Thus, z is the coordinate normal to the ferroelectric surface (Fig. 1). The potential produced by a dipole is:

$$\Phi(\mathbf{r}) = \frac{\mathbf{p}\cdot\hat{\mathbf{r}}}{4\pi\epsilon_0 r^2}. \tag{2}$$

The potential energy felt by an electron situated at (x, y, z) in empty space may be obtained by integrating the potential of the dipole density over the whole area of the ferroelectric.

$$V(x,y,z) = -\frac{ePdz}{4\pi\epsilon_0}\int_{-l}^{l} dx_0 \int_{-l}^{l} \times \frac{dy_0}{\{(x-x_0)^2 + (y-y_0)^2 + z^2\}^{3/2}}. \tag{3}$$

Integrating firstly over y_0, then over x_0 (see the Supplemental Material S1.1), one obtains:

$$V(x,y,z) = -\frac{ePdz}{4\pi\epsilon_0}\sum_{s,t=\pm1}(-1)^{s+t}\tan^{-1} \times \frac{(x+sl)(y+tl)}{z\sqrt{(x+sl)^2+(y+tl)^2+z^2}}. \tag{4}$$

The consistency of this formula for regions such as $y < -l$, $-l \leqslant y \leqslant l$, and $y \geqslant l$ has been checked. The function is even in x and y, $V(x,y,z) = V(x,-y,z) = V(-x,y,z)$, and symmetric when x and y are exchanged, $V(x,y,z) = V(y,x,z)$. In the origin ($x = y = z = 0$), one obtains:

$$V(0,0,0) \equiv V_0 = -\frac{ePd}{2\epsilon_0} \tag{5}$$

whereas when $z \to \infty, V \to 0$. Thus, the surface band bending as felt by an electron from vacuum is given by equation (5). Let us recall the band bending near the surface inside the ferroelectric layer, given by Eq. (1), with δ being the distance between the surface and the layer of mobile carriers contributing to the screening of the depolarization field. Several initial hypotheses may be formulated: (a) If these band bendings were equal, $d = 2\delta/\epsilon_r$. δ is estimated to be in the range of 2–30 nm [2], ϵ_r in the range of 50–200, thus $d = 0.2-12$ Å. Thus d may be close to either a few lattice parameters or even to the ionic displacements inside the unit cell in the polarized state. (b) By setting $d = \delta$ or even $d =$ the thickness of the whole film implies huge values of V_0. In any case, d cannot be attributed to the whole thickness of the ferroelectric film (10–100 nm), since then one may estimate $V_0 \approx 570$–5700/eV. The analysis of experimental LEED patterns and especially the dependence of V_0 on the thickness of the film will help us to decide on the interpretation of d.

The next step is to simplify the problem by computing the potential energy and the equation of motion for an escaping electron in a median plane of the sample (assuming that this plane contains the LEED spots of interest), e.g., ($y = 0$). In this case:

$$V_m(x,z) = V(x,0,y) = -\frac{ePdz}{2\pi\epsilon_0}\left\{\tan^{-1}\left[\frac{l(x+l)}{z\sqrt{l^2+(x+l)^2+z^2}}\right] - \tan^{-1}\left[\frac{l(x-l)}{z\sqrt{l^2+(x-l)^2+z^2}}\right]\right\}. \tag{6}$$

Surface and contour plots of this potential energy dependence in the vicinity of the sample surface may be seen in the SM, S1.2, Fig. SM-1 [49].

The forces (axial, i.e., z component, and tangential, i.e., x component) are computed as:

$$F_z(x,z) = -\frac{\partial V_m}{\partial z}$$
$$F_x(x,z) = -\frac{\partial V_m}{\partial x} \tag{7}$$

with complete formulas given in the SM, S1.3. One may easily check that $F_x(-x,z) = -F_x(x,z)$ and $F_z(-x,z) = F_z(x,z)$, as required by the symmetry of the problem.

Assuming that the electron is scattered at an angle θ with respect to the surface normal, the trajectory may be determined by integrating the Newton equations of motion (t being the time elapsed from the impact with the surface, m the mass of the electron):

$$x(t) = v_0 t\sin\theta + \frac{1}{m}\int_0^t dt' \int_0^{t'} dt'' F_x(x(t''),z(t''))$$
$$z(t) = v_0 t\sin\theta + \frac{1}{m}\int_0^t dt' \int_0^{t'} dt'' F_z(x(t''),z(t'')). \tag{8}$$

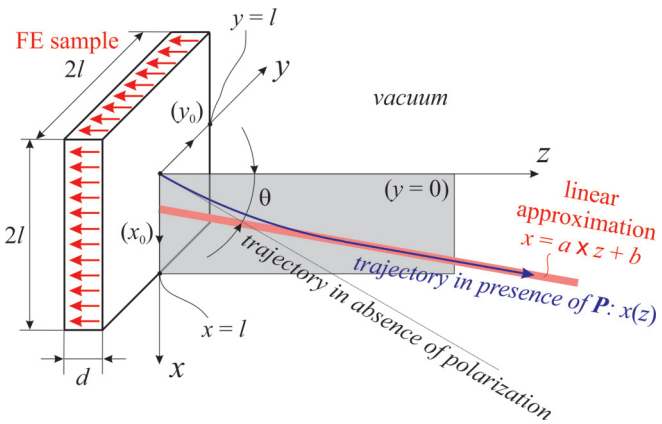

FIG. 1. Relevant parameters of a ferroelectric sample viewed as a distribution of dipoles and its influence on the trajectory of an outgoing electron.

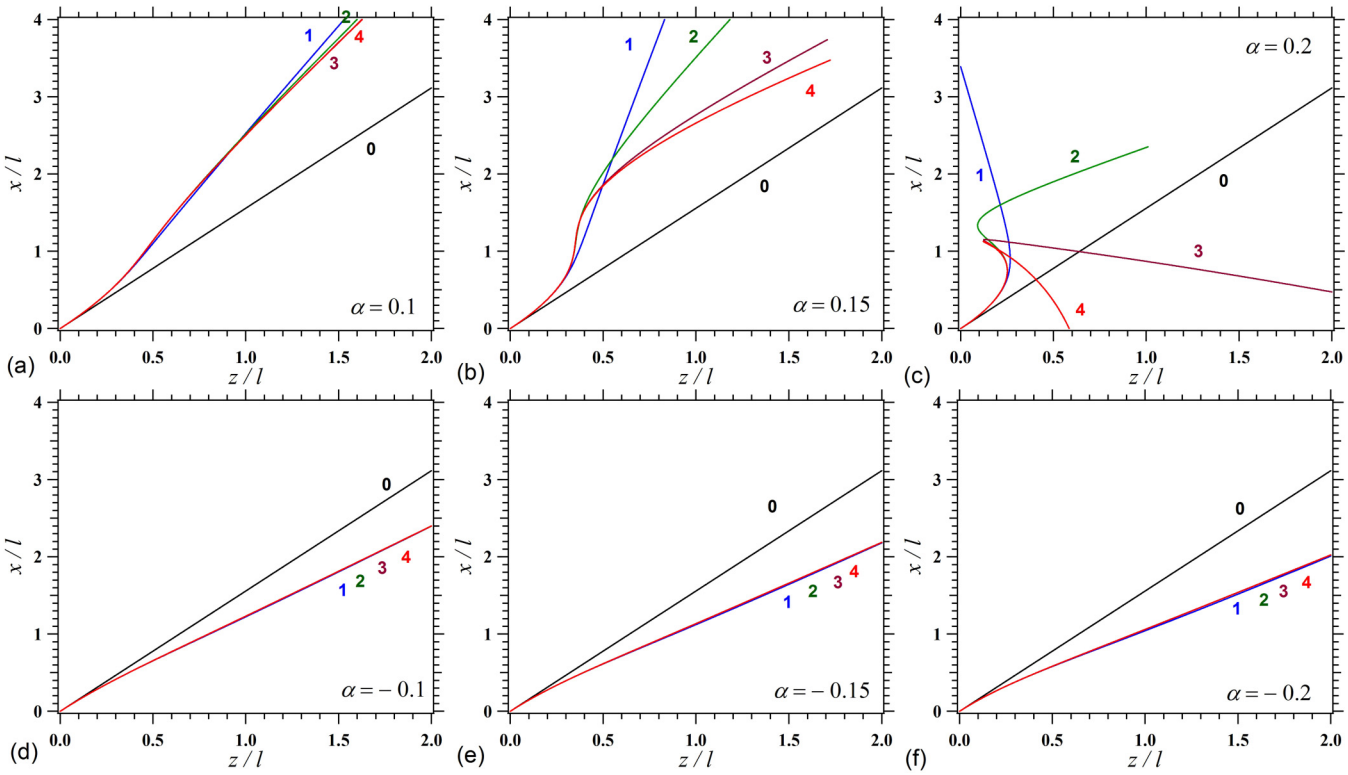

FIG. 2. First successive iterations for solving the coupled equations of motion (9), for $\theta = 1$ rad. and different values of the parameter α.

We assumed that the electron beam is well focused on the center of the sample, which coincides with the center of the LEED screen, such that the origin of the trajectory along the x axis $x_0 = 0$.

The next step is to use more convenient units and to write the problem with a minimum number of parameters. A natural unit for spatial (x and z) coordinates is l. A natural unit for time is $\tau = l/v_0$, where v_0 is the speed of the electron. Introducing the electrons kinetic energy at the impact with the surface E_0, $\tau = l(\frac{m}{2E_0})^{1/2}$. In these dimensionless parameters, the equations of motion are written as:

$$x(t) = t\sin\theta + \alpha\int_0^t dt'\int_0^{t'} dt''\, f_x(x(t''),z(t''))$$
$$z(t) = t\sin\theta + \alpha\int_0^t dt'\int_0^{t'} dt''\, f_z(x(t''),z(t'')), \qquad (9)$$

where

$$f_x(x,z) = z(1+z^2)\left\{\frac{1}{h_+(x,z)j_+(x,z)} - \frac{1}{h_-(x,z)j_-(x,z)}\right\}$$
$$f_z(x,z) = \frac{(x-1)[h_-(x,z)^2+z^2]}{h_-(x,z)j_-(x,z)} - \frac{(x+1)[h_+(x,z)^2+z^2]}{h_+(x,z)j_+(x,z)} \qquad (10)$$

and

$$h_\pm(x,z) = \sqrt{1+(x\pm 1^2)+z^2};$$
$$j_\pm(x,z) = z^2+(x\pm 1)^2(z^2+1)+z^4.$$

Thus, the trajectory, obtained by solving Eqs. (9), will be defined by the angle θ and by the dimensionless parameter α, defined as:

$$\alpha = \frac{ePd}{2\pi\epsilon_0 m v_0^2} = -\frac{V_0}{2\pi E_0} = -\frac{V_0}{2\pi(E-V_0)}. \qquad (11)$$

This parameter, up to the $1/(2\pi)$ factor, is the ratio between the surface potential energy and the kinetic energy at the impact point. The energy conservation was used $E = E_0 + V_0$, and E is the energy of the emitted electron by the LEED system. The emission point ($x = 0, z = z_e$), i.e., the end of the electron gun (in units of l), is assumed to be situated at a large distance from the sample ($z_e \gg 1$ in l units), otherwise an additional term derived from Eq. (6) has to be introduced to account for the potential energy produced by the ferroelectric surface at the electron emission point:

$$\alpha = -\frac{V_0}{2\pi\left\{E + \frac{2V_0}{\pi}\cot^{-1}\left(z_e\sqrt{2l^2+z_e^2}\right) - V_0\right\}}. \qquad (12)$$

From the fundamental point of view, the problem is solved; the trajectories may be obtained from the coupled integral equations (9). The system may be solved by iterations. Starting with a zero order trajectory $x^{(0)}(t) = t\sin\theta$ and $z^{(0)}(t) = t\cos\theta$, introducing these dependencies in the integrals in the right hand side of Eqs. (9), by numerical integration one obtains the solutions from a first iteration $x^{(1)}(t)$ and $z^{(1)}(t)$, then these solutions are re-introduced in the integral, the second order solutions are calculated, etc. Figure 2 presents the way these solutions converge for three different values of α and for $\theta = 1$ rad. Note that for $\alpha \geqslant 1/(2\pi)$ the trajectories become quasichaotic and the iteration procedure cannot be used. According to Eq. (11), this corresponds to the case where

the initial total energy of the electron $E = E_0 + V_0$ becomes negative, thus, such situations are not physical.

For a reasonable range of parameters α and θ, the convergence is ensured after five iterations, with a precision much better than the experiments may provide. Plots of trajectories obtained for several scattering angles θ and for two different values of the α parameter are also given in Fig. SM-1.

B. Approximations

In practical cases, the distance from the center of the sample to the LEED screen (R) is considerably higher than the sample lateral size ($2l$). In these conditions, the last part of the electrons trajectory (towards the screen) may be approximated by a straight line (Fig. 1). Also, the LEED screen itself is not grounded, but set to a high accelerating voltage (5–6 kV). Towards the sample one finds one or two earthed grids screening the potential of the screen, and, towards the LEED system one finds a retarding grid. The strong radial field for electron deceleration occurs between the (last) earthed grids and the retarding grid, and the acceleration between the retarding grid and the screen does not affect the shape of the electron trajectory, already assumed linear at such high distances from the sample. Figure SM-2 from S1.4 presents a real case, for relatively elevated values of α and θ. Thus, for computing the intersection of the trajectory with the LEED screen, the linear approximation is suitable. Hence, the simulation consists of the following steps:

(i) Solve by iterations equations (9) for several values of α and θ as parameters; the result will consist of trajectories, i.e., functions $x(\alpha,\theta;z)$.

(ii) Fit the obtained functions for large values of x and z with straight lines $x(\alpha,\theta;z) \approx a(\alpha,\theta) + b(\alpha,\theta)\cdot x$; derive numerically the dependencies $a(\alpha,\theta)$ and $b(\alpha,\theta)$; this complete procedure was achieved for $0.01 \leqslant \theta \leqslant 1$ rad. and $-0.35 \leqslant \alpha \leqslant 0.15$. According to Eq. (11), this corresponds to $E > 1.45V_0$ for $V_0 > 0$ and to $E > 0.06|V_0|$ for $V_0 < 0$. Some results are given in Fig. SM-3. As expected, $a(\alpha = 0,\theta) = 0$ and $a(\alpha,\theta = 0) = 0$. Also, $b(\alpha = 0,\theta) = \tan\theta$, as proven by Fig. SM-4(b). Thus, $\tan\theta$ can be naturally factorized from $b(\alpha,\theta)$. For practical reasons, and also in order to satisfy $a(\alpha,\theta = 0) = 0$, we will factorize $\tan\theta$ also from $a(\alpha,\theta)$.

(iii) Find analytical approximations for $a(\alpha,\theta)$ and $b(\alpha,\theta)$; this will be realized in two steps: (iii.1) fit, for each θ, $a(\alpha,\theta)$ and $b(\alpha,\theta)$ with convenient (known) functions of α and of $p+1$ parameters $f_a(c_0^{(a)}(\theta),...,c_p^{(a)}(\theta);\alpha)$ and $f_b(c_0^{(b)}(\theta),...,c_p^{(b)}(\theta);\alpha)$. The empirically derived function, which fits well both $a(\alpha,\theta)$ and $b(\alpha,\theta)$ as a function of α, for a wide range of θ, was (including the above factorization of $\tan\theta$):

$$a,b \approx f_{a,b}\left(c_0^{(a,b)},c_1^{(a,b)}(\theta),...,c_4^{(a,b)}(\theta),\alpha\right) = \frac{c_0^{(a,b)} + c_1^{(a,b)}(\theta)\alpha + c_2^{(a,b)}(\theta)\alpha^2}{1 + c_3^{(a,b)}(\theta)\alpha + c_4^{(a,b)}(\theta)\alpha^2}\tan\theta, \qquad (13)$$

where $c_0^{(a)} = 0$ and $c_0^{(b)} = 1$, in order to satisfy $a(\alpha = 0,\theta) = 0$ and $b(\alpha,\theta = 0) = \tan\theta$. Figure SM-4 presents selected fits for $a(\alpha,\theta)$ and $b(\alpha,\theta)$, for $\theta = 0.01,0.1,0.2,...,1$ rad.

TABLE I. Coefficients $\beta_{kj}^{(a)}$.

		k →			
		1	2	3	4
	0	–0.19777	1.1658	–8.2537	17.57
	1	–0.0021268	–0.22304	1.2631	–2.2614
	2	–0.19067	15.849	–82.621	187.79
	3	–0.17034	–102.3	553.85	–1250.1
j	4	–0.34974	369.46	–1978.7	4744.3
	5	2.8685	–797.7	4232.9	–10673
↓	6	–5.9601	1066	–5614.2	14712
	7	6.4201	–865.27	4532.5	–12234
	8	–3.5145	391.75	–2042.5	5640.4
	9	0.78788	–75.819	393.91	–1105.2

(iii.2) find analytical approximations for the eight parameters $c_1^{(a,b)}(\theta),...,c_4^{(a,b)}$. The most versatile empirical formula proposed, which may be used for all eight dependencies, is a polynomial of the ninth degree:

$$c_k^{(\mu)}(\theta) \approx \sum_{j=0}^{9} \beta_{kj}^{(\mu)}\theta^j, \qquad (14)$$

where $\mu = a,b$, and the $(2\times 4\times 10)$ coefficients $\beta_{kj}^{(a,b)}$ yielded the values from Tables I and II. The corresponding fits of the parameters $c_j^{(a,b)}(\theta)$ are represented in Fig. SM-5.

Once again, the trajectories at large distance from the ferroelectric surface may be approximated by straight lines $x = a + b\cdot z$, where the coefficients a and b depend on θ and α by the formulas (13) and (14) using the coefficients from Tables I and II. The whole problem is then well approximated for $0 \leqslant \theta \leqslant 1$ rad. and $-0.35 \leqslant \alpha \leqslant 0.15$ by the use of the 80 coefficients $\beta_{kj}^{(a,b)}$.

(iv) Find the intersection with the LEED screen, considered as a spherical cap placed at the distance R from the center of the sample, i.e., $x^2 + z^2 = (R/l)^2$. Introducing the linear trajectory $x = a + b\cdot z$, the solution is:

$$z_1(R/l,\alpha,\theta) = \frac{\sqrt{[b(\alpha,\theta)^2+1](R/l)^2 - a(\alpha,\theta)^2} - a(\alpha,\theta)b(\alpha,\theta)}{b(\alpha,\theta)^2+1} \qquad (15)$$

TABLE II. Coefficients $\beta_{kj}^{(b)}$.

		k →			
		1	2	3	4
	0	–7.9487	8.3112	–9.6047	19.424
	1	0.1502	2.2238	0.031638	1.9065
	2	–7.609	–47.828	–6.0285	–24.782
	3	127.4	367.37	103.77	113.05
j	4	–891.7	–1416	–782.26	336.25
	5	3200.6	2614.1	2921.7	–3575.4
↓	6	–6244.3	–2083.3	–5837.7	9847.1
	7	6730.8	91.466	6388.2	–12630
	8	–3781.5	800.54	–3626.1	7879.8
	9	866.41	–328.14	836.83	–1934.2

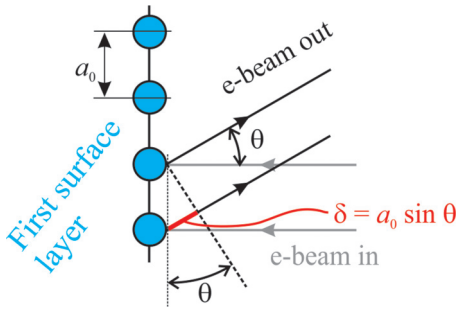

FIG. 3. Diffraction condition on two rows of atoms. δ is the path difference between electron wave functions scattered on neighboring atoms. Adapted from Ref. [58].

and

$$x_1(R/l,\alpha,\theta) = \sqrt{(R/l)^2 - z_1(\alpha,\theta)^2}, \tag{16}$$

where, once again, x_1 and z_1 are dimensionless, i.e., measured in l units.

When the distance to the LEED screen is much larger than the sample size, $R \gg l$, and/or the sample presents inwards polarization, $V_0 > 0$ and $\alpha < 0$ [then, according to Fig. SM-4(a), $a < 0.05$], the above formulas may be simplified to yield:

$$x_1(R,\alpha,\theta) \approx \frac{Rb(\alpha,\theta)}{l\sqrt{1+b(\alpha,\theta)^2}}. \tag{17}$$

For practical reasons, the values which will be analyzed will be scaled to the radius of the screen R_0, which may be expressed as function of the viewing angle ($2\theta_0$) by:

$$R_0 = R\sin\theta_0 \tag{18}$$

so, finally, the measured distances on the LEED screen, normalized to its radius, are to be expressed as:

$$\xi = \frac{lx_1}{R_0} = \frac{\sqrt{1-\left\{\frac{l}{R}z_1(R/l,\alpha,\theta)\right\}^2}}{\sin\theta_0} \tag{19}$$

or, for $R \gg l$, and/or inwards polarization ($\alpha < 0$):

$$\xi = \frac{lx_1}{R_0} \approx \frac{b(\alpha,\theta)}{\sin\theta_0\sqrt{1+b(\alpha,\theta)^2}}. \tag{20}$$

The parameter θ is not a free parameter, it is defined by diffraction conditions, involving the in-plane distance between rows of atoms a_0. According to Fig. 3 (rows are oriented perpendicular to the plane of the image), coherence (i.e., the apparition of a LEED spot) is realized when the path difference satisfies:

$$\delta = a_0\sin\theta_0 = n\lambda = \frac{nh}{p} = \frac{nh}{\sqrt{2mE_0}} = \frac{nh}{\sqrt{2m(E-V_0)}} \tag{21}$$

or, again, if one considers also the potential energy at the emission point of the electron, as in Eq. (12):

$$\delta = \frac{nh}{\sqrt{2m\left\{E + \frac{2V_0}{\pi}\cot^{-1}\left(z_e\sqrt{2l^2+z_e^2}\right) - V_0\right\}}}, \tag{22}$$

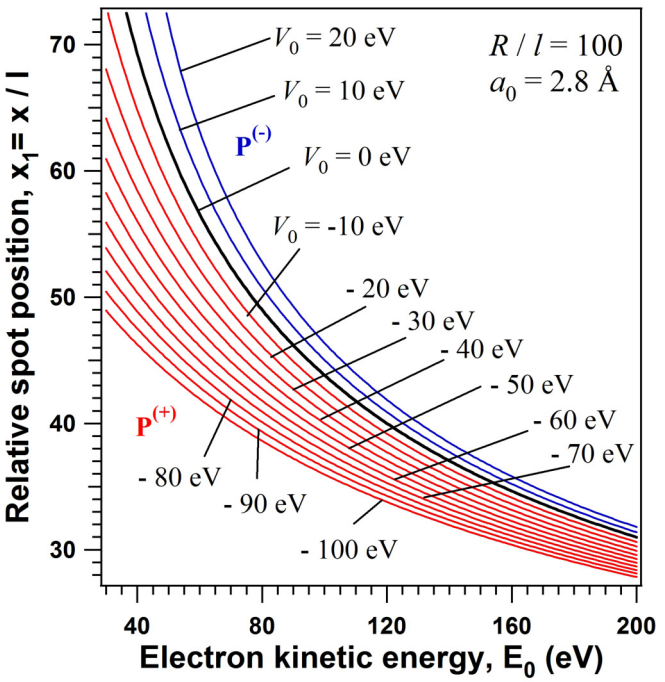

FIG. 4. Position of LEED spots x_1 vs kinetic energy, for fixed R/l and several values of V_0.

where n is the order of the spot, h the Planck constant, and λ the electron associated wavelength. Thus,

$$\sin\theta = \frac{nh}{a_0\sqrt{2mE_0}} \approx \frac{12.271n}{a_0[\text{Å}]\sqrt{E-V_0[\text{eV}]}} \tag{23}$$

or

$$\sin\theta = \frac{nh}{a_0\sqrt{2mE_0}} \approx \frac{12.271n}{a_0[\text{Å}]\sqrt{\left\{E + \frac{2V_0}{\pi}\cot^{-1}\left(z_e\sqrt{2l^2+z_e^2}\right) - V_0\right\}[\text{eV}]}}. \tag{24}$$

Of course, these formulas contain implicitly lower bounds for E_0 for a LEED spot to appear, even at large deflection angles (close to 90°).

Thus, the dependence of the position of the LEED spots x_1 vs the electron kinetic energy (E) is to be simulated with Eqs. (15), (19), or (20), where θ is given by Eq. (23) or (24), $a(\alpha,\theta)$ and $b(\alpha,\theta)$ are given by Eqs. (13), (14) with the coefficients $\beta_{kj}^{(a,b)}$ from Tables I and II, and α is given by Eq. (11) or (12). The variables of the model are E, θ_0, a_0, l/R, and V_0. In principle, R and θ_0 are known from the LEED manufacturers specification, l is also known [the sample lateral size; it will not be needed, nor R, if Eq. (20) is used for the spot positions, in the approximation $l \ll R$ and/or $V_0 > 0$] and a_0 should also be known from other determinations of the sample crystal structure. The only variable in the fit remains V_0, therefore a few points (kinetic energies) might be sufficient to determine it. Some simulations of $x_1(R/l,E_0,V_0,a_0)$ are given in Fig. 4, for $a_0 = 2.8$ Å and several values of V_0. The result is at variance with the trajectories represented in Fig. SM-1, in the sense that for $P^{(+)}$ polarized surfaces the LEED pattern is

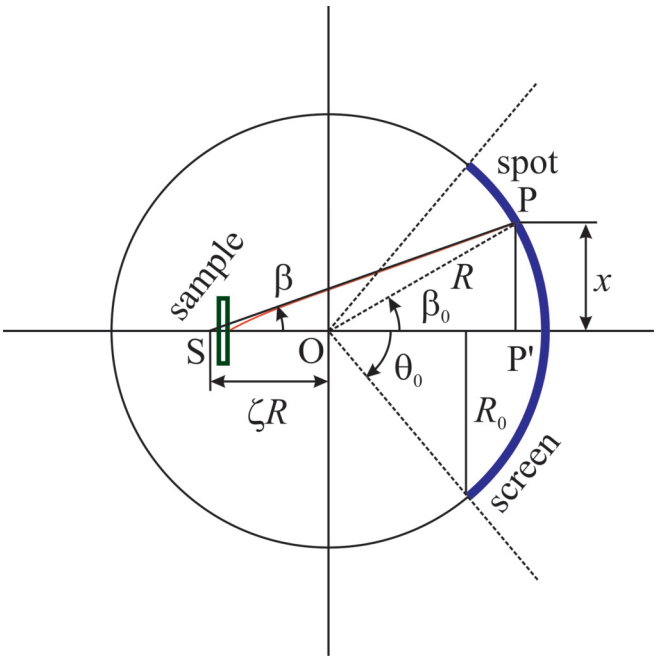

FIG. 5. Relevant parameters for assessing geometry effects due to the deviation of the surface position from the center of the LEED system.

shrinking whereas for $P^{(-)}$ it is expanding. The reason for that is the presence of V_0 at the denominator of Eq. (23) or (24). The diffraction condition involves the kinetic energy near the surface, where the electron is subject to the potential energy V_0. For a positive polarization $P^{(+)}$, V_0 is negative and the kinetic energy increases near the surface; thus, the diffraction spots correspond to electrons emitted at lower angles. Despite the fact that the trajectories are spread afterwards, as in Fig. SM-1(a), the effect of lower diffraction angles prevails with respect to the case of unpolarized surfaces, $V_0 = 0$.

Some geometric parasitic effects must also be discussed. The sample orientation is relatively easily achieved, provided a sample manipulator with sufficient degrees of freedom is used (polar rotation and tilt); what is more difficult is to place the sample surface such that the center of the sphere of radius R is contained in its surface plane. Thus, the last point to be modeled concerns the effect of a deviation of the sample position from this point, following the direction of the incoming electron beam, as represented in Fig. 5, for the simplified case $R \gg l$, and/or $V_0 > 0$. $\beta = \tan^{-1} b$ is the apparent emission angle, obtained from the large distance (straight line) trajectory. Note that $a \approx 0$. The sine theorem in the triangle POS yields:

$$\frac{R}{\sin\beta} = \frac{\zeta R}{\sin(\beta_0 - \beta)}. \tag{25}$$

The position of the LEED spot $|\,PP'| \equiv x$ is given (in real units, i.e., not normalized with respect to l) by:

$$\begin{aligned} x &= R\sin\beta_0 = R\sin\{\beta + \sin^{-1}(\zeta\sin\beta)\} \\ &= R\sin\beta\{\sqrt{1-\zeta^2\sin^2\beta} + \zeta\cos\beta\} \\ &= R\frac{b(\alpha,\theta)\{\sqrt{1+b(\alpha,\theta)^2(1-\zeta^2)}+\zeta\}}{1+b(\alpha,\theta)^2}. \end{aligned} \tag{26}$$

Finally, the formula to be used in the following is obtained by combining Eq. (26) with (18):

$$\xi = \frac{lx_1}{R_0} \equiv \frac{x}{R_0} \approx \frac{b(\alpha,\theta)\{\sqrt{1+b(\alpha,\theta)^2(1-\zeta^2)}+\zeta\}}{\sin\theta_0\{1+b(\alpha,\theta)^2\}}. \tag{27}$$

The parameters of the model are (i) the viewing angle of the LEED system θ_0, (ii) the relative deviation of the sample surface from the center of the LEED system ζ, (iii) the in-plane distance between rows of atoms defining the LEED spot a_0, and (iv) the surface potential energy V_0.

III. EXPERIMENTAL SECTION

A. Experimental

All experiments were performed in two similar ultrahigh vacuum (UHV) clusters, the first one (A) consisting of (i) a molecular beam epitaxy (MBE) chamber with standard sample preparation techniques (annealing in UHV, ion sputtering, evaporators), LEED (Specs ErLEED 150), reflection high energy electron diffraction (RHEED) and Auger electron spectroscopy (AES); (ii) a photoemission chamber with dual anode x-ray gun (Al/Mg K_α), monochromatized Al K_α source, a 150 mm radius electron energy analyzer, He UV lamp and, again, ion sputtering and sample heating facilities; (iii) a variable-temperature scanning tunneling microscopy (STM) chamber. The second cluster (B) is the experimental endstation of the SuperESCA beamline at the Elettra synchrotron radiation facility, Trieste. It has a preparation chamber and a chamber for analyses by photoelectron spectroscopy using synchrotron radiation, where also LEED patterns may be recorded by using a Vacuum Generators RVL900 device. The base pressure in all chambers is in low 10^{-10} mbar or even 10^{-11} mbar range. X-ray photoelectron spectra are obtained in both setups by using similar Phoibos 150 mm electron energy analyzers; in the setup (A), monochromatized Al K_α radiation (1486.74 eV) was used; in the setup (B), variable energy synchrotron radiation provided by the SuperESCA beamline was used.

p-doped $[(0.8-6)\times 10^{17}\ \mathrm{cm}^{-3}]$ Ge(001) wafers are routinely cleaned by several (2–3) cycles of annealing at 650 °C during 30 minutes in a vacuum not exceeding 1×10^{-9} mbar. No oxygen or carbon contamination is detected by XPS. STM reveals the (2×1) reconstruction. XPS spectra recorded were standard for clean Ge(001) $p(2\times 1)$. More details about the sample preparation and characterization by other techniques (XPS, STM) can be found in previous work [50,51].

$Pb(Zr_{0.2}Ti_{0.8})TiO_3(001)$ (PZT) thin films were produced by PLD by using a KrF laser. The complete setup and preparation conditions are described in Refs. [3,10]. The samples analyzed in this work were deposited on $SrRuO_3$ (SRO) or $LaSrMnO_3$ (LSMO) as bottom electrodes, grown on $SrTiO_3(001)$ also by PLD. Three samples were analyzed by LEED and XPS: (a) a 10 nm thick PZT film grown on SRO/STO(001), analyzed in the setup (A) described above; (b) a 50 nm thick PZT film grown on SRO/STO(001), analyzed in the setup (B) described above; a 100 nm thick PZT film grown on LSMO/STO(001), analyzed in the setup (B). After synthesis, the samples were investigated by piezoresponse force microscopy (PFM) and showed single domain structure with polarization oriented

outwards (S2, Figs. SM-6 and SM-7 for the films with 50 and 100 nm, respectively). The PLD preparation facility is not connected *in situ* with ultrahigh vacuum clusters; nevertheless, a cleaning procedure was set up by annealing for 3–6 hours in 5×10^{-5} mbar O_2 pressure at 400 °C [19,21]. This annealing procedure is performed in steps of two hours, by checking the sample stoichiometry and the carbon contamination after each step. The final result of this procedure is a good stoichiometry derived by XPS, e.g., $Pb(Zr_{0.2}Ti_{0.8})TiO_{\sim 2.84}$. Thus, there are oxygen vacancies in the films, as expected, necessary to screen the depolarization field [18]. It is supposed that upon this cleaning procedure the single-domain character of the films is kept, even if the polarization is reversed, otherwise XPS spectra would have shown peaks at different binding energies corresponding to areas with different orientation of the polarization.

The samples, with lateral sizes of 5×5 mm^2 are mounted for both experiments discussed here (LEED and XPS) on Mo sample holders, by using Mo plates and screws, and these plates touch the surface at its extremities. The effect of surface charging was tested during the photoemission experiments by varying the flood gun intensity and a very weak shift (below 0.2 eV) was observed between spectra recorded without using the flood gun and spectra recorded with a flood gun current of up to 2 mA. Also, XPS was recorded using the SuperESCA beamline with $(0.3 - 1.0) \times 10^{12}$ photons/sec. on a spot of 10×100 μm. This implies a total electron yield emitted from the sample of at least 50 nA, or at least 50 μA/mm^2. This flux is by two orders of magnitude higher than the flux used in LEED experiments. Nevertheless, no significant deviations in measured binding energies are detected. More recently, an experiment was performed on the Spectromicroscopy beamline at Elettra on 50 nm PZT/LSMO(001) by using a photon flux of 1.5×10^{11} photons/sec. on a circular spot of 0.6 μm diameter, and this corresponds to a photoemitted charge of at least 85 mA/mm^2 [52]. In this experiment, the photon flux was sufficient to induce surface dissociation within a few minutes, but still no significant shift in binding energies was observed.

All samples are extensively characterized by x-ray diffraction, piezoresponse force microscopy, electrical measurements (see Ref. [18]), and ferroelectric hysteresis to prove their ferroelectricity [an example of $P(E)$ hysteresis loop is presented in S3, Fig. SM-8].

B. Data analysis

LEED images are recorded with CCD cameras and corrected for possible camera aberrations, such that the contour of the LEED screen is well fit by a circle. LEED images are analyzed by extracting spot profiles along directions connecting opposite (0,1) with $(0,\bar{1})$; (1,1) with $(\bar{1},\bar{1})$ or (0,2) with $(0,\bar{2})$ spots, see S4 (Fig. SM-9). Then, the regions corresponding to peaks are simulated with Voigt profiles [53] together with quadratic backgrounds. Voigt profiles are used in order to discriminate between coherence lengths and electron beam spot profile [54]. This allows us to determine the distance between symmetric spots. The coherence length obtained from the spot profile analysis is in the range of 11 ± 3 nm. Special care was undertaken to determine the (circular) radius of the LEED screen, both from analyses of spot profiles, or directly from images. At the end, an average value obtained from all images with the same LEED system was used to normalize the position of the LEED spots. After this procedure, the normalized values of ξ were fit with formula 27. In fact, since in this work two experiments [Ge(001) and 10 nm PZT(001)] were performed with one LEED system (Specs ErLEED 150) and two other experiments [50 nm and 100 nm PZT(001)] are performed with another LEED system (VG RVL900), there is a common fitting parameter ζ for the series of images obtained with the same system, since physically the surfaces were located in the same position, up to tiny differences in thickness between the Ge(001) wafer and the STO(001) substrate. Thus, the positions of the LEED spots were simulated simultaneously by pairs of experiments. The viewing angle θ_0 was fixed (42° for the first system and 52° for the second). In order to check the reproducibility of the fit, 10 000 fits were performed for each pair of data, and at the end the series of values for each parameter were subject to standard statistical analysis to yield the average value and the standard deviation. This procedure produced the values listed in Tables III and IV.

TABLE III. Fitting parameters obtained for Ge(001). The left column represent parameters obtained by fitting with $V_0 = 0$, fixed.

Parameter	Ge(001)	
a_0 (Å)	3.997 ± 0.090	*3.99*
θ_0 (degrees)	42.0	*40.5*
V_0 (eV)	1.083 ± 0.431	*0*
ζ	-0.020 ± 0.021	*−0.05*

The XPS data were fitted with Voigt profiles summed up with their primitive functions [53]. For doublets (Pb 4f, Zr 3d, Ti 2p), formulas used for fit are given in Ref. [52]. We took also into account branching ratios and Coster-Kronig effects on different Lorentzian widths from a doublet for Ti 2p [55]. Also for Ti 2p, the spectra obtained with monochromated Al K_α radiation have also a contribution from a broad Pb Auger line [9]. The integral intensities (over the whole doublet, if any) were normalized with respect to the synchrotron radiation flux [19] and to the photoionization cross sections [56] to yield relative atomic concentrations, which were afterwards normalized for unit (Zr + Ti) content. The effective inelastic mean free path (IMFP) in synchrotron radiation experiments was quite low (in the range of $\lambda \cos\varphi = 5.3$ Å, where λ is the IMFP and $\varphi = 40°$ the take-off angle), therefore deviations in the $p = \text{Pb}(\text{Zr} + \text{Ti})^{-1}$ ratio may be partially ascribed to IMFP effects combined with PbO (for $p > 1$) or $(\text{Ti,Zr})O_2$ termination (for $p < 1$). More details on this kind of analysis may be found in Ref. [19]. As a consequence (see Table IV), it seems that the 10 nm sample is $(\text{Ti,Zr})O_2$ terminated, and for the other two samples the outer monoatomic layer is PbO.

IV. RESULTS

A. General aspects. A nonferroelectric surface: Ge(001)

The relevant parameter that will be discussed in the following is the surface potential energy V_0 of a distribution of dipoles over the sample surface, see Eq. (5). We know from the

TABLE IV. Relevant fitting parameters from the LEED patterns of three PZT(001) surfaces. Error bars are computed from a "multifit" procedure consisting of performing 10 000 times the fit with random initial parameters (roughly ±10 % from the expected vales for a_0 and ±100 % from the expected values for V_0 and ξ). Binding energy values corresponding to the maxima of the Pb $4f_{7/2}$, Zr $3d_{5/2}$, Ti $2p_{3/2}$, and O $1s$ XPS spectra are also given (see also Fig. 8 and Figs. SM-12, SM-13 and SM-14) to account for the $P^{(-)}$ polarization of these films. The carbon contamination represents the integral intensity of the C $1s$ peak (Fig. SM-15) divided by integral intensities of all other peaks, with proper observation of the photoionization cross sections (Ref. [56]) and of the undulator flux for experiments performed using synchrotron radiation. Binding energies, degrees of contaminations, and compositions are given only for the annealed samples (first and second annealing, respectively); compositions do not take into account inelastic mean free path effects.

Sample Parameter	PZT(001), 10 nm/SRO	PZT(001), 50 nm/SRO	PZT(001), 100 nm/LSMO
a_0 (Å)	3.852 ± 0.086	3.780 ± 0.149	3.818 ± 0.173
V_0 (eV)	8.978 ± 0.489	6.730 ± 2.448	10.618 ± 4.344
ζ	0.020 ± 0.022	0.105 ± 0.035	
Pb $4f_{7/2}$ (eV)	138.28	137.67	138.46
	137.79	137.27	137.31
Zr $3d_{5/2}$ (eV)	182.21	181.83	181.09
	181.64	180.69	180.64
Ti $2p_{3/2}$ (eV)	458.63	458.32	457.80
	458.01	457.15	457.17
O $1s$ (eV)	529.93	530.50	530.00
	528.72	528.69	529.35
C contamination (%)	<0.5	6.36	5.33
	< 0.5	4.96	2.47
Approximate compositions	$Pb_{0.45}Zr_{0.21}Ti_{0.79}O_{2.77}$ $Pb_{0.45}Zr_{0.20}Ti_{0.80}O_{2.84}$	$Pb_{1.47}Zr_{0.18}Ti_{0.82}O_{2.05}$ $Pb_{1.79}Zr_{0.25}Ti_{0.75}O_{2.80}$	$Pb_{1.48}Zr_{0.17}Ti_{0.83}O_{1.85}$ $Pb_{2.08}Zr_{0.16}Ti_{0.84}O_{2.72}$

very beginning, see the Introduction and Eq. (1), that dipoles whose field is not compensated by the accumulation of mobile charges will exist only in a thin layer near the outer surface of the ferroelectric. Thus, the unknown value of d will rather represent the parameter δ from Eq. (1). From the analysis of the energy variation of the distance between the LEED spots, one will derive V_0, i.e., the product (Pd) and from the value of the surface band bending derived from XPS one will derive the factor $(P\delta\epsilon_r{}^{-1})$. Once the analysis procedure will be achieved, we shall comment on the validity of the assumption $d = \delta$. Other parameters are a_0, the distance in real space associated to the LEED spot, the viewing angle of the LEED optics θ_0, and the relative deviation of the sample position from the center of the LEED system ζ.

We start with the analysis of a nonferroelectric sample. LEED images obtained for Ge(001) are presented in Fig. 6. The result of the fit of LEED spot positions is presented in Fig. 7. The parameters obtained are $a_0 = 4.00$ Å (in good agreement with the surface lattice constant $2^{-1/2}a = 5.658\sqrt{2}$ Å), $2\theta_0 = 84^\circ$ (practically the same as the technical specification of the ErLEED optics), and $V_0 = 1.08$/eV (though highly scattered, 1.08 ± 0.43/eV). The diffracted electrons are subject to a repelling force from the surface, which may be due to a difference in work function between the filament and the sample. The LEED filament is, by construction, made on low work function materials (at most 3.5–4 eV), such as to operate at lower temperatures. The sample is grounded, therefore the Fermi level is the same from the filament to the sample. A higher work function in the sample together with energy conservation means that the kinetic energy (above the vacuum level) is lower at the sample by the difference in work function, which is the value of V_0 obtained by fit.

All fitting parameters are listed in Table III. Fitting by fixing $V_0 = 0$ yielded also a good fit, with reasonable parameters (θ_0, a_0, ζ).

We anticipate that a similar effect generated by work function difference might occur also for PZT samples, but their work function could exceed that of germanium by at most 1 eV [57]. Consequently, if the surface potential energies for ferroelectric samples obtained from the actual analysis are exceeding 2 eV, this effect may be attributed to polarization effects.

B. Lead zirco titanate PZT(001)

Figure 8 presents LEED images obtained on 100 nm PZT/SRO/STO(001), while the series of LEED patterns obtained on other PZT films are presented in S5 (Figs. SM-10 and SM-11). Figure 9 analyzes spatial distributions of the LEED spots vs electron kinetic energy for all PZT films. The values of $2\theta_0$ are fixed from the technical specifications of the LEED systems [84° for setup (A) and 104° for setup (B)]. The fitting parameters are $a_0 = 3.85$ Å for 10 nm, 3.78 Å for 50 nm, and 3.82 Å for 100 nm PZT/LSMO/STO(001), close to the relaxed in-plane lattice constant of 3.916 Å measured by high resolution transmission electron microscopy for 100 nm thick films prepared by the same technique [11]; the most important parameter in this study $V_0 = 8.98$, 6.73, and 10.62 eV. The parameter ζ is negligible in experiments with the setup (A) and has a relatively low value for the setup (B): about 0.1, which implies a perpendicular deviation of the position of the sample surface $\zeta R_0 \approx 5.5$ mm from the center of the sphere extrapolating the LEED screen. All fitting parameters are listed in Table IV, together with error bars; the modality to determine

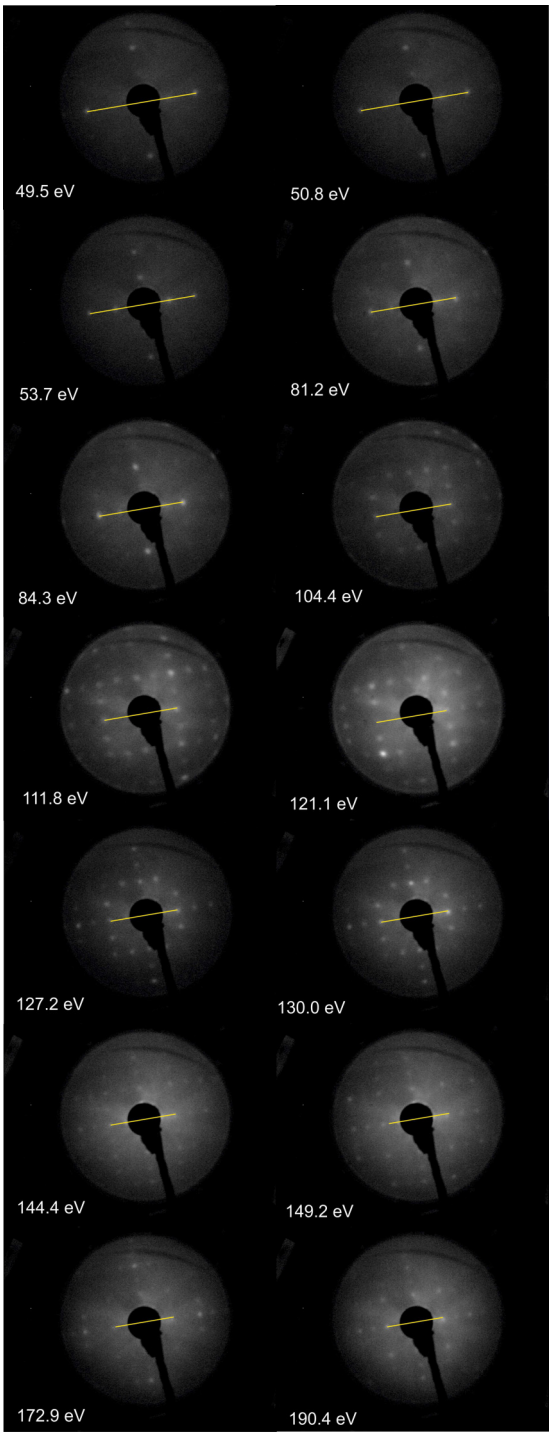

FIG. 6. LEED patterns obtained on Ge(001) at electron energies specified on each panel, by using a Specs ErLEED 150. Yellow lines indicate distances between (01) and ($0\bar{1}$) spots.

these error bars is discussed in the Methods section. Fitting with $V_0 = 0$ fixed does not give reasonable parameters, as discussed in S6.

C. X-ray photoelectron spectroscopy

XPS spectra (Pb 4f: Fig. 10, Zr 3d: Fig. SM-12, Ti 2p: Fig. SM-13, O 1s: Fig. SM-14) revealed the presence of

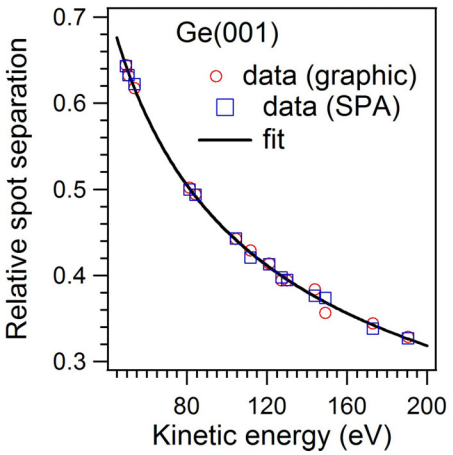

FIG. 7. Fit of the spacing between (01) spots of Ge(001) by using Eqs. (13), (14), and (27).

$P^{(-)}$ polarization states for samples treated at least two times (2 hours) in O_2 atmosphere (5×10^{-5} mbar), prior to the LEED analysis. Irrespective if the first annealing is performed in vacuum or in oxygen, this creates oxygen vacancies and then stabilizes the $P^{(+)}$ polarization state [18], while the films still exhibit a slight carbon contamination. As reported previously [19], when the surface becomes free of contaminants, the $P^{(-)}$ state is stabilized. We recall that the 10 nm sample seems to be (Ti,Zr)O_2 terminated, while the other PZT samples seem to be PbO terminated, from the amplitude ratios of Pb/(Zr + Ti). However, the fact that similar values for V_0 are obtained for 10 nm and for 100 nm thick films imply that the surface termination or the film thickness do not play a significant role in the value of the surface potential energy. The lower value obtained for the surface potential energy in the case of the 50 nm film could be related to a higher degree of carbon contamination of the samples (about 5% for this sample, as compared with about 2.5% for the 100 nm film and below the detection limit for the 10 nm film, see Fig. SM-15).

V. DISCUSSIONS

The values obtained for V_0 are consistent with the hypothesis of perturbation of electron trajectories by the ferroelectric. Using Eq. (5) with $P \sim 0.8 - 1$ Cm^{-2}, one obtains $d \approx$ 1.2–2.3 Å, lower or on the order of half of the out-of-plane lattice parameter, $c/2$, and at least one order of magnitude below the parameter δ derived previously for this sample composition (∼20 Å) [2].

In fact, the relevant parameter obtained from the actual theory is the product Pd, which can be regarded as a surface dipole density $Pd = 2\epsilon_0 V_0 e^{-1} = p a_0^{-2}$, where p is the dipole moment corresponding to a surface elementary cell (understood as a sum of all net dipole moments lying beneath the surface, not compensated by the mobile charge sheets). One obtains $p \approx 1.1$–1.7 eÅ, lower than the dipole moment corresponding to an elementary cell of about 3.0–3.9 eÅ for $P = 0.8 - 1$ Cm^{-2}. Two mechanisms may explain these findings: (a) the dipole moment near the surface is considerably smaller than its value in the bulk, derived by macroscopic

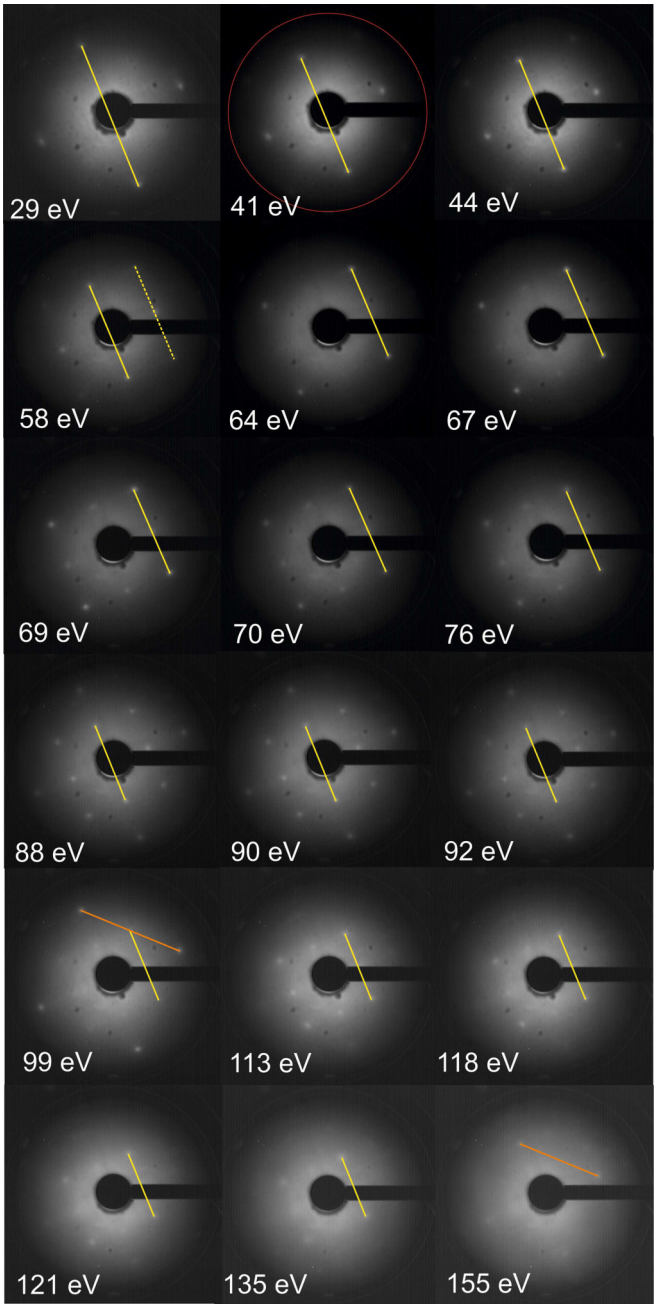

FIG. 8. LEED patterns obtained on a 100 nm PZT/$LaSrMnO_4$(001) surface, at electron energies specified on each panel, using a VG RVL900 setup. Yellow lines figure distances between (01) and $(0\bar{1})$ spots, or between (11) and $(1\bar{1})$ spots. Orange lines figure distances between $(0\bar{2})$ and (20) spots, which are $\sqrt{2}$ times bigger. The red circle on one panel figures the diameter of the screen R_0.

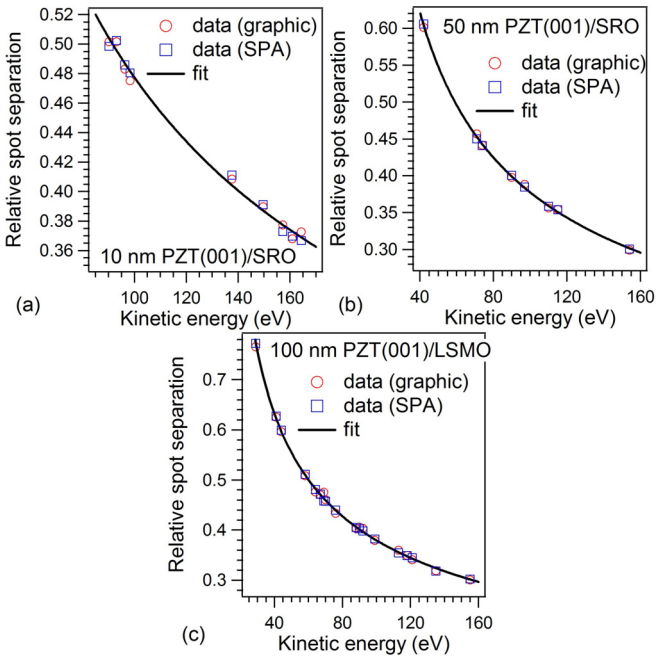

FIG. 9. Fit of the spacing between (01) spots of PZT(001) by using Eqs. (13), (14), and (27). (a) 10 nm PZT/SRO/STO(001), setup (A); (b) 50 nm PZT/SRO/STO(001), setup (B); (c) 100 nm PZT/LSMO/STO(001), setup (B). The red circles are spot positions extracted from a graphic analysis in a graphic software of distances between spots; blue squares are values obtained from the LEED spot profile analysis. The points obtained by the latter procedure were fitted.

P–V measurements; (b) the screening of the dipole distribution occurs immediately near the surface.

From XPS, we infer differences in binding energies between $P^{(+)}$ and $P^{(-)}$ states of about 1.2 eV, which implies that the band bending inside the film is of about $V_B = eP\delta\epsilon^{-1} \approx 0.6$/eV. Introducing macroscopic polarizations of 0.8–1 Cm^{-2} [3,18], (see also S7) the ratio $\delta{\epsilon_r}^{-1} \approx 5.3 - -6.6 \times 10^{-2}$ Å is obtained. The assumption that $\delta = d$ (from the actual model) ≈1.8 Å may be justified by a much lower value of the dielectric constant $\epsilon_r \approx 27$–34. If the real polarization of the outer layers is decreasing by a factor of 2–2.5, as derived from photoelectron diffraction [43] or by first principles calculations [34], the whole model fits better with a dielectric constant of about 54–85. Note that a similar value was inferred at room temperature from the temperature dependence of the polarization-related molecular adsorption [19] or for 'dead layers' of ferroelectrics with metal contacts [35,36,58,59]. Also, in the Introduction we mentioned an early work deriving the thickness-independent 'intrinsic' dielectric constant for $PbZr_{0.2}Ti_{0.8}O_3$ is of about 27–56 [27], together with similar values estimated theoretically [25] or derived by Raman spectroscopy [26]. This is in agreement also with recent simulations of the I–V characteristics for ferroelectric capacitors [58]. However, the thickness of the 'dead layer' in previous studies ranged from 5–8 Å to 2–4 nm. Assuming a thickness of 3 unit cells (about 12 Å) for the 'dead layer' inside the PZT film, then the relative permittivity in the 'dead layer' would be of about 145, very similar to the value obtained from C–V measurements [30]. In this case, the 'dead layer' appears to be a part of the depletion layer existing at the surface/interface of ferroelectric films. A model based only on Schottky type contacts can simulate relatively well the C–V characteristics [59], but fails to simulate the I–V ones. Given the low thickness of the 'dead layer,' in spite of its low dielectric constant, its capacity is large enough to not affect the simulation of the C–V characteristics, as for the case of the I–V

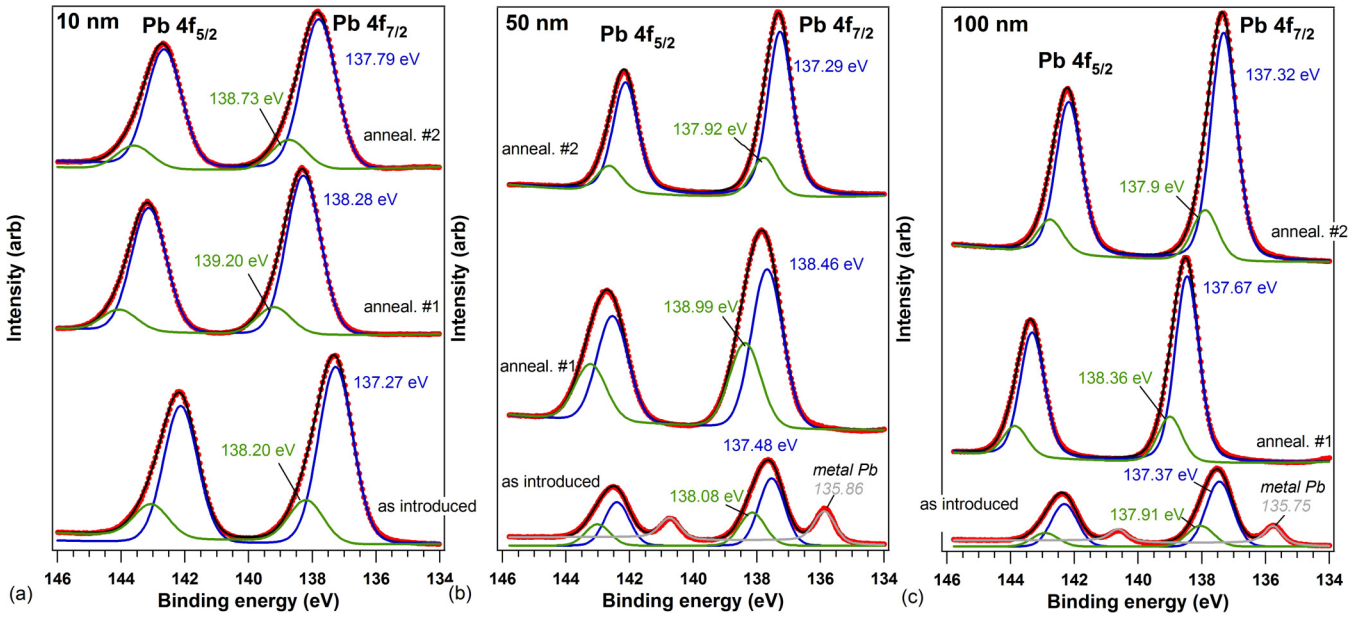

FIG. 10. Pb 4f x-ray photoelectron spectroscopy: (a) 10 nm PZT/$SrRuO_3$/$SrTiO_3$(001); (b) 50 nm PZT/$SrRuO_3$/$SrTiO_3$(001); (c) 100 nm PZT/ $LaSrMnO_4$/$SrTiO_3$(001) for *as introduced* samples and after two annealing cycles. (a) is obtained by using monochromatized Al K_α radiation (photon energy $h\nu = 1486.74$/eV), while (b),(c) are obtained using synchrotron radiation with $h\nu = 260$/eV. All spectra are corrected by the Fermi energy using an Au foil. The spectra are fit with Voigt doublets and associated integral backgrounds yielding the binding energies of the $4f_{7/2}$ maxima, specified in each graph. Artificial intensity offsets are introduced for clarity.

characteristics, where injected electrons are very sensitive to interface properties. One can infer that the value extracted from LEED experiments represents a lower limit for the thickness of the 'dead layer' inside a ferroelectric with the surface in ultrahigh vacuum. The thickness of the 'dead layer' may be larger if an electrode is deposited, due to inherent interface states and structural defects altering the potential landscape and the polarization gradient near the interface.

From the actual analysis, a low value of the product $P\delta \approx Pd = 2\epsilon_0 V_0$ is derived. For a nonuniform variation of the polarization with thickness $P(z)$ for $z < 0$, and taking into account also the depolarization charge density $\rho(z)$, this product can be written as:

$$'Pd' \equiv \int_{-\infty}^{0} \left\{ P(z) - \int_{-\infty}^{z} \rho(z')dz' \right\} dz = 2\epsilon_0 V_0 \qquad (28)$$

whereas the inner potential energy (band bending) (1), taking into account also the variation of the dielectric constant, can be expressed as:

$$'V_B' \equiv -\frac{e}{\epsilon_0} \int_{-\infty}^{0} \frac{1}{\epsilon_r(z)} \left\{ P(z) - \int_{-\infty}^{z} \rho(z')dz' \right\} dz. \qquad (29)$$

An electrostatic model of a ferroelectric near its free surface should then start with a microscopic modeling of the interdependency of its polarization $P(z)$ and polarizability [i.e., dielectric constant $\epsilon_r(z)$ *via* the Lorentz-Lorenz equation] on the charge density, given by free carriers and/or ionized impurities, together with the dependence of these charge densities on the potential energy $V(z) = -e\phi(z)$ (using usual statistics from semiconductor physics), introduce all dependencies in the Poisson equation with sources $\mathrm{div}(\epsilon\nabla\phi + P) = \rho$ and solve it with appropriate boundary conditions [60].

We obtained also a discrepancy by one order of magnitude between the inner potential energy V_B and the outer potential energy V_0. We note by $\Delta V = V_0 - V_B$. It is reasonable to suppose that this discontinuity is extended over a given distance η. The field in this region may be regarded as produced by two parallel charge sheets with a surface density σ [eÅ^{-2}] $\approx 0.55 \times 10^{-3} \Delta V$ [eV] η^{-1}[Å]. For $\Delta V = 10.6 - 0.6 = 10.0$/eV, a value of $\eta \approx 0.8$ Å yields about $1e$ by $a_0{}^2$. If ions were responsible for the negative charge implied to yield such a strong value of ΔV, then their photoelectron spectra should result in unusually low binding energies. Since no component in XPS was visible at such a low binding energy, the only reasonable hypothesis is the formation of an electron gas on the vacuum side of the film. The positive charge should be formed by the last layer of cations (Pb^{2+}, Ti^{4+}, or Zr^{4+}); note also that the variation of binding energies of Ti $2p$ and Zr $3d$ follows that of Pb $4f$ binding energies, see S7 (Figs. SM-12 and SM-13). The electron layer can be connected to a large amount of oxygen vacancies in the first layer. This may also explain why clean layers feature $P^{(-)}$ polarization: For the opposite situation to occur, one needs to form a sheet of positive charges outside the film, which can be produced only in ions (e.g., from contaminating molecules). Indeed, C $1s$ signals shifted by 4–5/eV towards larger binding energies are visible quite often on partly contaminated films exhibiting $P^{(+)}$ polarization, and are usually attributed to O–C=O complexes [61]; it may happen that such components are in fact just ionized carbon within the positive charge sheet to stabilize the single domain $P^{(+)}$ polarization. As mentioned above, such screening mechanisms involving contaminants were proposed alternately with respect to the internal screening by mobile charges [12,13]. For the case of $P^{(+)}$ layers of PZT(001), an early work detected Pb $5d$ components at 8.9 eV higher binding

energies [8], attributed to areas with incomplete compensation of the depolarization field, but which might also be asserted to ionized Pb atoms from the surface.

Consequently, the actual value of surface potential energies are in line with Eq. (5), with the d parameter close to the distance between two consecutive layers. These values are, as stated in the Introduction, almost two orders of magnitude larger than the differences in kinetic energies corresponding to MEM–LEEM transitions [21–24]. If some charge screening occurs, it should be the same for electrons used in a LEED or in a LEEM device. The main differences between the actual experiments and LEEM experiments from Refs. [21–24] are: (i) the kinetic energy of the electrons used (30–200/eV in the actual experiments, a few eV or even fractions of eV in MEM–LEEM experiments); (ii) the electron spot size (0.2–1 mm in the actual experiments, in the range of 1 μm for LEEM) and, consequently, possible order of magnitude variations in the electron flux; (iii) the fact that the actual samples presented uniform polarization, whereas in the above references LEEM was recorded on patterned areas by PFM on multidomain samples.

We start with the third difference: Reference [21] analyzed a surface subject to PFM writing of a pattern consisting of a 10×10 μm^2 $P^{(-)}$ area with a 5×5 μm^2 $P^{(+)}$ area written in a smaller square with the same center as the first, while the polarization imprint of the remaining area is $P^{(+)}$; Refs. [22] and [23] analyzed surfaces presenting stripes of about 10 μm width with alternate polarizations; Ref. [24] analyzed four adjacent (on the longest edge) $P^{(-)}/P^{(+)}/P^{(-)}/P^{(+)}$ PFM areas of 5×20 μm^2, with no imprint on the remaining area. Now, one needs to acknowledge the fact that the electron dynamics extend on a macroscopic scale, of at least 10 mm, much larger than typical sizes of domains or of PFM polarized areas. As a consequence, at large distances from the surface, electrons are subject to similar average potentials. Differences in the potential occur only at distances in the μm range. The complete analysis will be detailed in a further work, however here we sketch some of the preliminary results. Starting with the complete spatial dependence of the potential given by Eq. (4), we were able to construct the z dependence of the potential when electrons are driven towards the center of the $P^{(+)}$ written area or on the $P^{(-)}$ area. Near the sample, the $P^{(-)}$ area exhibit a continuously increasing potential energy of height $|V_0|$, measured with respect to the potential of the area with imprint polarization, whereas the $P^{(+)}$ area exhibits a local maximum of amplitude $\sim 0.5|V_0|$ quite close to the surface (at about 2.75 μm out of the surface). The difference yielded in the repelling potential energy near the surface is therefore $0.5|V_0| = ePd(4\epsilon_0)^{-1}$, and not $2ePd\epsilon_0{}^{-1}$, as stated in Ref. [24]. Then, almost one order of magnitude from the discrepancy may be gained by this evaluation. However, the derived d is still in the range of 0.035 Å for $P = 0.7 - 1\ \mathrm{Cm}^{-2}$; in order to accommodate with a value in the range of 1 Å, one needs to suppose a drastic decrease of the polarization, by a factor 20–35.

We may also discard effects connected to the electron flux variation between both experiments. It was shown, for instance, in Ref. [23], that UV irradiation reduces the energy difference between MEM–LEEM transitions from 400 to 90 meV. The power of the UV lamp (20 $\mathrm{mW\,cm}^{-2}$) and its wavelength (254 nm) allows one to estimate a flux of about 2.5×10^{20} photons ($\mathrm{s}^{-1} \times \mathrm{m}^{-2}$), while the electron flux for LEED experiments is in the range of 1 μA mm^{-2} $\equiv 6.25 \times 10^{18}$ electrons ($\mathrm{s}^{-1} \times \mathrm{m}^{-2}$). For the LEEM experiments of Ref. [48], about 2.1×10^{19} electrons ($\mathrm{s}^{-1} \times \mathrm{m}^{-2}$) were shown to induce polarization switching at surfaces of $BaTiO_3$ single crystals. There is a factor of 12–40 between these fluxes from UV irradiation and electron-based experiments, if one assumes that most UV photons are transformed into electrons. At the same time, none of the Refs. [21–24] reported instabilities during the electron irradiation of the sample. Let us remind also the stability of binding energy in spectromicroscopic experiments performed with huge photon flux, about 5.3×10^{11} photons/($\mathrm{s} \times \mu\mathrm{m}^2$), which yields a photoemitted electron flux of at least some tens of mA per mm^2 [52].

The first difference, the kinetic energy of the employed electrons, should affect mainly their penetration depth inside the sample. But a nontrivial, though fundamental, problem of quantum mechanics occurs. It is easy to compute that the de Broglie associated wavelength of these electrons varies with their kinetic energy (E_0) such as $\lambda_B[\mathrm{nm}] \approx 1.23 \times (E_0[\mathrm{eV}])^{-1/2}$. At the MEM–LEEM transition, electrons will have a low kinetic energy, thus it is reasonable to suppose that their associated de Broglie wavelength might approach the range of strong variation of the potential (fractions of μm). As a consequence, this potential will be perceived as "smoothed" by the low energy electrons and hence the barriers might be reduced. We must also think that the potential energy landscape is represented by a strong variation extending over a quite limited depth (δ being a few/AA). Electrons which should capture such variations will then have associated de Broglie wavelengths at least in this range, and these will be LEED electrons with kinetic energies in the range of 100 eV. Electrons with kinetic energies below 1 eV will have associated wavelengths exceeding by more than one order of magnitude δ. Supposing, to simplify, that the origin of V_0 is represented by two metal planes set at this potential energy difference, separated by δ, an electron with $\lambda_B \gg \delta$ will feel just the average potential of these two planes. A somehow similar problem occurs in a crystal, where electrons in the valence bands with de Broglie wavelengths in the nm range are not sensitive to strong variations of the ionic cores, manifesting in the range of sub-Ångström distances (the "jellium" model).

Therefore, the small energy differences from MEM–LEEM transitions may be attributed to a combined influence of dead layers with lower polarization, dynamical screening, or effects related to the delocalization of very low energy electrons over spatial ranges exceeding the range of potential energy variation. In the LEED experiments, the electron wavelength is considerably smaller (in the Å range) and fine potential variations in the near-surface region manifest more readily.

An alternative way to detect surface potential energy variations is Kelvin probe microscopy (KPM) [62]. By using a scanning probe microscope (SPM) allowing KPM to operate in ultrahigh vacuum, atomically clean ferroelectric surfaces could also be investigated. However, if the surface presents uniform polarization, absolute work function data are more difficult to be extracted, the technique being sensitive mainly to

changes of work function values; thus, one should think about pre-writing well-defined patterns on the surface, as in PFM [19] (see also S2). Also, SPM systems operating in ultrahigh vacuum are more expensive than usual LEED optics by about one order of magnitude. Finally, it may happen that, since KPM operates by small potential differences near the Fermi energy, its depth resolution will be limited, such as in the case of MEM–LEEM transition, and this technique might be unable to detect potential energy variation on a scale of a few Å, as LEED electrons are able to visualize. Nevertheless, one may think that, taking into account the actual improvement of preparation conditions for ferroelectric single crystal films, in short time KPM experiments will be performed on ferroelectric films with out-of-plane polarization and of convenient cleanness to detect the properties of the ferroelectric film itself.

VI. CONCLUSION

We derived the potential energy produced by a distribution of localized dipole moments emulating a ferroelectric film of thickness d and computed the trajectories of electrons reflected by the surface. The position of the LEED spots is obtained as a function of the electron kinetic energy, with a surface potential energy, as seen by LEED electrons, which may be expressed as $V_0 = -ePd(2\epsilon_0)^{-1}$. Fitting the position of the LEED spots vs electron kinetic energies and knowing the polarization of the sample allows one to derive the parameter d, which is unusually low (below 2 Å) for practical cases analyzed, ferroelectric PZT(001) films of different thicknesses. If this parameter d is interpreted as being similar to the distance from the surface to the sheet formed by mobile charge carriers to screen the depolarization field inside the ferroelectric (δ), then the surface band bending inside the ferroelectric may be accommodated with this low value of d by using a quite low value of the dielectric constant, of 30 ± 4, or in the range 27–85 if one allows also a decrease of the polarization. This implies either (a) that the whole material, in the absence of metal contacts and other interface effects or traps, has a low dielectric constant (along the c axis) or (b) that 'dead layers' with low values of dielectric constants and/or polarization are manifesting *even in ultrathin samples and for free ferroelectric surfaces*. Also, the value of the external potential energy may be explained by the formation of a double charge sheet over the surface of the ferroelectric, involving free electrons located on the vacuum side. This suggests also why clean layers presented the polarization oriented inwards, while most contaminated films present outwards polarization, since for the last case to occur one needs a support (such as adsorbed molecules) to accommodate positive charges.

These results are all obtained on thin ferroelectric films, and it seems that the values of the surface potential energies are rather insensitive to the film thickness, but more sensitive to the presence of some adsorbates on the surface. Thin, single domain, ferroelectric films undergo the 'self-doping' phenomenon [18] in order to create oxygen vacancies and to generate electrons together with ionized donors to compensate the depolarization field. These generated electrons are most probably the origin of the negative charge sheet we supposed on the surface in order to explain the discrepancies between potential energy outside and inside the film. An open question is what will happen in the case of thick films or single crystals, where most probably the self-doping is less effective and a much lower density of defects is needed to generate the same surface charge density, if and only if single domain states may be synthesized. Normally, the formation of the negative charge sheet on the surface should occur also in this case, but, up to its experimental confirmation, we cannot anticipate more on this subject. Also, one may seek for the future the adaptation of the present results to a formalism integrated in the analysis of LEED I–V curves, by taking into account the strong potential energy variations near a ferroelectric surface.

ACKNOWLEDGMENTS

Access to the Elettra synchrotron radiation facility was provided by the Proposal No. 20155416. Consistent support from Silvano Lizzit, Polo Lacovig, and Luca Bignardi during the experiments at Elettra is gratefully acknowledged. This work is funded by the Romanian Ministry of Research and Innovation through the Core Programme, Project No. PN16-480103/2016, and by the UEFISCDI Agency through the Project No. PN-II-RU-TE-2014-4-0456.

[1] L. Pintilie and M. Alexe, J. Appl. Phys. **98**, 124103 (2005).
[2] L. Pintilie, I. Boerasu, M. J. M. Gomes, T. Zhao, R. Ramesh, and M. Alexe, J. Appl. Phys. **98**, 124104 (2005).
[3] I. Pintilie, C. M. Teodorescu, C. Ghica, C. Chirilă, A. G. Boni, L. Hrib, I. Pasuk, R. Negrea, N. Apostol, and L. Pintilie, ACS Appl. Mater. Interfaces **6**, 2929 (2014).
[4] F. Chen, R. Schafranek, W. B. Wu, and A. Klein, J. Phys. D **44**, 255301 (2011).
[5] F. Chen and A. Klein, Phys. Rev. B **86**, 094105 (2012).
[6] N. G. Apostol, L. E. Ştoflea, G. A. Lungu, C. A. Tache, D. G. Popescu, L. Pintilie, and C. M. Teodorescu, Mater. Sci. Eng., B **178**, 1317 (2013).
[7] L. E. Ştoflea, N. G. Apostol, L. Trupină, and C. M. Teodorescu, J. Mater. Chem. A **2**, 14386 (2014).
[8] D. G. Popescu, M. A. Huşanu, L. Trupină, L. Hrib, L. Pintilie, A. Barinov, S. Lizzit, P. Lacovig, and C. M. Teodorescu, Phys. Chem. Chem. Phys. **17**, 509 (2015).
[9] N. G. Apostol, L. E. Ştoflea, G. A. Lungu, C. Chirilă, L. Trupină, R. F. Negrea, C. Ghica, L. Pintilie, and C. M. Teodorescu, Appl. Surf. Sci. **273**, 415 (2013).
[10] L. E. Ştoflea, N. G. Apostol, C. Chirilă, L. Trupină, R. Negrea, L. Pintilie, and C. M. Teodorescu, J. Mater. Sci. **49**, 3337 (2014).
[11] N. G. Apostol, L. E. Ştoflea, L. C. Tănase, I. C. Bucur, C. Chirilă, R. F. Negrea, and C. M. Teodorescu, Appl. Surf. Sci. **354**, 459 (2015).
[12] M. A. Khan, M. A. Nadeem, and H. Idrissn, Surf. Sci. Rep. **71**, 1 (2016).
[13] A. Kakekhani, S. Ismail-Beigi, and E. I. Altman, Surf. Sci. **650**, 302 (2016).
[14] S. V. Kalinin, C. Y. Johnson, and D. A. Bonnell, J. Appl. Phys. **91**, 3816 (2002).
[15] C. Baeumer, D. Saldana-Greco, J. M. P. Martirez, A. M. Rappe, M. S. Shim, and L. W. Martin, Nat. Commun. **6**, 6136 (2015).

[16] A. Rajapitamahuni, J. Hoffman, C. H. Ahn, and X. Hong, Nano Lett. **13**, 4374 (2013).

[17] X. Hong, J. Hoffman, A. Posadas, K. Zou, C. H. Ahn, and J. Zhu, Appl. Phys. Lett. **97**, 033114 (2010).

[18] L. Pintilie, C. Ghica, C. M. Teodorescu, I. Pintilie, C. Chirilă, I. Pasuk, L. Trupină, L. Hrib, A. G. Boni, N. G. Apostol, L. E. Abramiuc, R. Negrea, M. Ştefan, and D. Ghica, Sci. Rep. **5**, 14974 (2015).

[19] L. C. Tănase, N. G. Apostol, L. E. Abramiuc, C. A. Tache, L. Hrib, L. Trupină, L. Pintilie, and C. M. Teodorescu, Sci. Rep. **6**, 35301 (2016).

[20] N. G. Apostol, G. A. Lungu, I. C. Bucur, C. A. Tache, L. Hrib, L. Pintilie, D. Macovei, and C. M. Teodorescu, RSC Advances **6**, 67883 (2016).

[21] I. Krug, N. Barrett, A. Petraru, A. Locatelli, T. O. Menteş, M. A. Niño, K. Rahmanizadeh, G. Bihlmayer, and C. M. Schneider, Appl. Phys. Lett. **97**, 222903 (2010).

[22] G. F. Nataf, P. Grysan, M. Guennou, J. Kreisel, D. Martinotti, C. L. Rountree, C. Mathieu, and N. Barrett, Sci. Rep. **6**, 33098 (2016).

[23] J. L. Wang, B. Vilquin, and N. Barrett, Appl. Phys. Lett. **101**, 092902 (2012).

[24] J. E. Rault, W. Ren, S. Prosandeev, S. Lisenkov, D. Sando, S. Fusil, M. Bibes, A. Barthélémy, L. Bellaiche, and N. Barrett, Phys. Rev. Lett. **109**, 267601 (2012).

[25] N. Sai, K. M. Rabe, and D. Vanderbilt, Phys. Rev. B **66**, 104108 (2002).

[26] J. A. Sanjurjo, E. López-Cruz, and G. Burns, Phys. Rev. B **28**, 7260 (1983).

[27] L. Pintilie, I. Vrejoiu, D. Hesse, G. LeRhun, and M. Alexe, Phys. Rev. B **75**, 224113 (2007).

[28] Q. Yang, J. X. Cao, Y. C. Zhou, L. H. Sun, and X. J. Lou, Acta Mater. **112**, 216 (2016).

[29] H. Yamada, A. Tsurumaki-Fukuchi, M. Kobayashi, T. Nagai, Y. Toyosaki, H. Kumigashira, and A. Sawa, Adv. Funct. Mater. **25**, 2708 (2015).

[30] P. Sun, Y. Z. Wu, S. H. Zhu, T. Y. Cai, and S. Ju, J. Appl. Phys. **113**, 174101 (2013).

[31] P. Maksymovych, M. Huijben, M. Pan, S. Jesse, N. Balke, Y.-H. Chu, H. J. Chang, A. Y. Borisevich, A. P. Baddorf, G. Rijnders, D. H. A. Blank, R. Ramesh, and S. V. Kalinin, Phys. Rev. B **85**, 014119 (2012).

[32] M. Stengel and N. A. Spaldin, Nature (London) **443**, 679 (2006).

[33] M. Stengel, D. Vanderbilt, and N. A. Spaldin, Nat. Mater. **8**, 392 (2009).

[34] M. Q. Cai, Y. Zheng, P. W. Ma, and C. H. Woo, J. Appl. Phys. **109**, 024103 (2011).

[35] L. W. Chang, M. Alexe, J. F. Scott, and J. M. Gregg, Adv. Mater. **21**, 4911 (2009).

[36] L. J. Sinnamon, R. M. Bowman, and J. M. Gregg, Appl. Phys. Lett. **78**, 1724 (2001).

[37] F. C. Sun, M. T. Kesim, Y. Espinal, and S. P. Alpay, J. Mater. Sci. **51**, 499 (2015).

[38] Y. Watanabe, Ferroelectrics **419**, 28 (2011).

[39] J. S. Shin, V. B. Nascimento, A. Y. Borisevich, E. W. Plummer, S. V. Kalinin, and A. P. Baddorf, Phys. Rev. B **77**, 245437 (2008).

[40] L. Despont, C. Koitzsch, F. Clerc, M. G. Garnier, P. Aebi, C. Lichtensteiger, J.-M. Triscone, F. J. G. de Abajo, E. Bousquet, and P. Ghosez, Phys. Rev. B **73**, 094110 (2006).

[41] M. Tachiki, M. Matsutani, T. Fujii, Y. Sakaguchi, and T. Kobayashi, Jpn. J. Appl. Phys. **34**, L1145 (1995).

[42] N. Bickel, G. Schmidt, K. Heinz, and K. Müller, Phys. Rev. Lett. **62**, 2009 (1989).

[43] A. Pancotti, J. Wang, P. Chen, L. Tortech, C.-M. Teodorescu, E. Frantzeskakis, and N. Barrett, Phys. Rev. B **87**, 184116 (2013).

[44] S. C. Bharath, K. R. Pimputkar, A. M. Pronschinske, and T. P. Pearl, Appl. Surf. Sci. **254**, 2048 (2008).

[45] S. Förster and W. Widdra, Surf. Sci. **604**, 2163 (2010).

[46] J. L. Wang, B. Vilquin, B. Gautier, G. Dezanneau, and N. Barrett, Appl. Phys. Lett. **106**, 242901 (2015).

[47] J. E. Rault, J. Dionot, C. Mathieu, V. Feyer, C. M. Schneider, G. Geneste, and N. Barrett, Phys. Rev. Lett. **111**, 127602 (2013).

[48] J. E. Rault, T. O. Menteş, A. Locatelli, and N. Barrett, Sci. Rep. **4**, 6792 (2014).

[49] See Supplemental Material at http://link.aps.org/supplemental/10.1103/PhysRevB.96.115438 for: S1. Addendum to the theoretical considerations on electrons diffracted from a ferroelectric surface. S2. Piezoresponse force microscopy. S3. Example of a ferroelectric hysteresis curve. S4. LEED spot profile analyses. S5. LEED patterns for 10 and 50 nm thick $Pb(Zr,Ti)O_3$ films grown on $SrRuO_3/SrTiO_3(001)$. S6. Comments regarding the analysis of the LEED patterns from PZT(001) with $V_0 = 0$, fixed. S7. Zr 3d, Ti 2p, O 1s, and C 1s x-ray photoelectron spectra.

[50] G. A. Lungu, L. E. Ştoflea, L. C. Tănase, I. C. Bucur, N. Răduţoiu, F. Vasiliu, I. Mercioniu, V. Kuncser, and C. M. Teodorescu, Materials **7**, 106 (2014).

[51] L. C. Tănase, A. E. Bocîrnea, A. B. Şerban, L. E. Abramiuc, I. C. Bucur, G. A. Lungu, R. M. Costescu, and C. M. Teodorescu, Surf. Sci. **653**, 97 (2016).

[52] L. E. Abramiuc, L. C. Tănase, A. Barinov, N. G. Apostol, C. Chirilă, L. Trupină, L. Pintilie, and C. M. Teodorescu, Nanoscale **9**, 11055 (2017).

[53] C. Teodorescu, J. Esteva, R. Karnatak, and A. E. Afif, Nucl. Instrum. Methods Phys. Res., Sect. A **345**, 141 (1994).

[54] R. M. Costescu, N. G. Gheorghe, M. A. Huşanu, G. A. Lungu, D. Macovei, I. Pintilie, D. G. Popescu, and C. M. Teodorescu, J. Mater. Sci. **47**, 7225 (2012).

[55] D. Luca, C. M. Teodorescu, R. Apetrei, D. Macovei, and D. Mardare, Thin Solid Films **515**, 8605 (2007).

[56] J. Yeh and I. Lindau, At. Data Nucl. Data Tables **32**, 1 (1985).

[57] C. Y. Wang, D. W. Cao, F. G. Zheng, W. Dong, L. Fang, X. D. Su, and M. R. Shen, Chem. Commun. **49**, 3769 (2013).

[58] L. D. Filip and L. Pintilie, Eur. Phys. J. B **89**, 44 (2016).

[59] L. D. Filip, L. Pintilie, V. Stancu, and I. Pintilie, Thin Solid Films **592**, 200 (2015).

[60] N. G. Apostol and C. M. Teodorescu, in *Surface Science Tools for Nanomaterials Characterization*, edited by C. S. S. R. Kumar (Springer, Berlin, Germany, 2015), Chap. 11, pp. 405–461.

[61] M. Iliuţ, C. Leordean, V. Cânpean, C. M. Teodorescu, and S. Aştilean, J. Mater. Chem. C **1**, 4094 (2013).

[62] W. Melitz, J. Shen, A. C. Kummel, and S. Lee, Surf. Sci. Rep. **66**, 1 (2011).